

Double half-Heusler alloys $X_2\text{Ni}_2\text{InSb}$ ($X = \text{Zr, Hf}$) with promising thermoelectric performance: The role of varying structural phases

Bhawna Sahni and Aftab Alam^{*}

Department of Physics, Indian Institute of Technology, Bombay, Powai, Mumbai 400076, India



(Received 23 February 2023; revised 25 July 2024; accepted 23 August 2024; published 12 September 2024)

Double half-Heusler (HH) alloys are a new class of compounds that can be seen as transmuted versions of two single half-Heusler alloys with higher flexibility of tunability of their properties. Here, we report a detailed study of the thermoelectric (TE) properties of two double HH alloys $X_2\text{Ni}_2\text{InSb}$ ($X = \text{Hf, Zr}$), using first-principles calculation. These alloys exhibit a rich phase diagram with the possibility of tetragonal, cubic, and solid-solution phases. As such, a comparative study of the TE properties of all these phases is highly desired. The simulated band gap, obtained using a hybrid functional, of the ordered phase of $\text{Hf}_2\text{Ni}_2\text{InSb}$ and $\text{Zr}_2\text{Ni}_2\text{InSb}$ lies in the range 0.24–0.4 and 0.17–0.59 eV, respectively, while, for the disordered phase, it lies in between 0.05 and 0.06 eV. A simulated TE figure of merit (ZT) as high as 2.02 and 2.45 is obtained for $\text{Hf}_2\text{Ni}_2\text{InSb}$ and $\text{Zr}_2\text{Ni}_2\text{InSb}$, respectively. In both compounds, electronic transport plays the dominant role in achieving the promising ZT values. We believe this study will attract the attention not only of experimentalists but also of theoreticians from the thermoelectric community to further investigate similar double HH alloys.

DOI: [10.1103/PhysRevApplied.22.034034](https://doi.org/10.1103/PhysRevApplied.22.034034)

I. INTRODUCTION

Thermoelectric technology that enables one to convert waste heat into electricity has proven to be extremely useful in providing solutions to renewable energy resources. Since most of the energy from primary sources is lost as waste heat, potential thermoelectric materials come to the rescue by harvesting this waste heat. The transport properties (Seebeck coefficient S , electrical conductivity σ , and thermal conductivity κ) that define the thermoelectric figure of merit (ZT) are closely interrelated, which makes it quite challenging to find novel materials with optimal ZT . Though several materials have been reported in the literature [1–9], the hunt for more efficient novel materials is still ongoing.

Half-Heusler (HH) alloys have emerged as promising thermoelectric (TE) materials due to a variety of interesting properties, such as good thermal stability, easily tunable band gaps, good mechanical properties, etc. [10–14]. They can be classified on the basis of their valence-electron count (VEC). The 18 valence-electron HH alloys are very stable because of fully occupied bonding and empty antibonding states. The 17 and 19 valence-electron HH alloys, on the other hand, are unstable because of partially occupied states. However, recent studies suggest stabilization of several compounds with 19 valence-electron count via defect manipulation. For example, in NbCoSb , the significant proportion of stable Nb vacancies

stabilizes the material by lowering the total electron count [15–17]. Mixing of a 17 and a 19 VEC HH alloy can also form an 18 VEC double half-Heusler alloy. These double half-Heusler alloys exhibit lower values of lattice thermal conductivity (κ_L) compared to their ternary counterpart because of smaller phonon group velocity and disorder scattering [18]. Apart from κ_L , if the electronic transport properties of these double HH alloys can be made more superior than those of the corresponding ternary systems, they can be very promising for TE applications. This is one of the motivation of the present work.

Anand *et al.* [18] explored a large number of previously unexplored double half-Heusler alloys and predicted many of them to be stable. The double half-Heusler compounds have the general formula unit $X_2YY'Z_2$, where Y and Y' are not isovalent, X is a transition metal, and Z is a main-group element. For example, the nominal non zero net valence ($NV \neq 0$) systems TiNiSb and TiFeSb are the two ternary components of the quaternary double half-Heusler compound $\text{Ti}_2\text{FeNiSb}_2$. The members TiFeSb , TiCoSb , and TiNiSb all have different net valence ($NV = -1, 0$, and 1, respectively). Anand *et al.* [18] showed that κ_L of double half-Heusler $\text{Ti}_2\text{FeNiSb}_2$ is lower in comparison to that of its corresponding ($NV = 0$) ternary counterpart TiCoSb (with the same average atomic mass) by a factor of 3 at room temperature. There are some reports on the effect of doping in these double half-Heuslers as well. For instance, Liu *et al.* [19] showed that by alloying Ti with Hf and by tuning the Fe:Ni ratio, a high figure of merit can be achieved for both *p*-type and *n*-type

*Contact author: aftab@iitb.ac.in

conduction in $\text{TiFe}_{0.5}\text{Ni}_{0.5}\text{Sb}$. Wang *et al.* [20] showed enhanced thermoelectric performance due to a very low value of thermal conductivity and high power factor in *p*-type double half-Heusler $\text{Ti}_{2-y}\text{Hf}_y\text{FeNiSb}_{2-x}\text{Sn}_x$ compounds. Recently, Hasan *et al.* [21] showed enhanced figure of merit in $\text{Ti}_2\text{FeNiSb}_{1.8}\text{Sn}_{0.2}$ as compared to the pristine $\text{Ti}_2\text{FeNiSb}_2$.

Since the ternary half-Heuslers ZrNiSn [10,11,22] and HfNiSn [11,12,23] have been widely studied for their promising thermoelectric performance, we chose to study the corresponding ($\text{NV} = 0$) double half-Heusler counterparts $\text{Zr}_2\text{Ni}_2\text{InSb}$ and $\text{Hf}_2\text{Ni}_2\text{InSb}$. Anand *et al.* [18] theoretically studied the Grüneisen parameter and thermal conductivity of these compounds in the tetragonal ($I\bar{4}2d$) structure as reported in the Open Quantum Materials Database (OQMD). Both these compounds, however, are experimentally reported to crystallize in cubic ($F\bar{4}3m$, #216) structure with few impurities, prepared under a specific processing condition [24,25].

We used first-principles calculations to investigate the electronic, phonon, and thermoelectric properties of the double half-Heuslers $\text{Zr}_2\text{Ni}_2\text{InSb}$ and $\text{Hf}_2\text{Ni}_2\text{InSb}$. In contrast to previous studies, we have simulated these properties of the two compounds in all of the three relevant phases, i.e., tetragonal, cubic, as well as solid solution. Depending on the synthesis condition and temperature, there is a possibility to realize all three of these phases, ordered at low temperature (T) while disordered in the high T range. Ordered structures could show higher carrier mobility than solid solution [26]. Thus, ordered structures with low lattice thermal conductivity (κ_L) can prove to be a better thermoelectric material. For an accurate estimate of band gap, the HSE06 [27] functional is used, which yields a band gap of 0.17 eV (0.59 eV) for the cubic (tetragonal) phase of $\text{Zr}_2\text{Ni}_2\text{InSb}$, while those for $\text{Hf}_2\text{Ni}_2\text{InSb}$ are 0.24 eV (0.4 eV). The corresponding solid-solution phase shows a narrow band gap of 0.05 and 0.06 eV for Zr- and Hf-based double HH alloys. Interestingly, these double HH alloys are found to show extremely high electronic transport (S , σ , and power factor), which actually makes them promising for TE application. The tetragonal phase is found to be the most promising candidate for TE applications, with figure of merit value as high as $ZT = 2.45$, at high T . The disordered phase is moderately promising because of the lowest values of lattice thermal conductivity. Such a comparative study of different structural phases of a single compound is extremely essential and useful to understand the nature of electron and phonon excitation in different T ranges.

II. COMPUTATIONAL DETAILS

We use the Vienna *Ab initio* Simulation Package (VASP) [28–30], within density functional theory [31], with a

projector augmented wave basis [32] and the generalized gradient approximation exchange-correlation functional of Perdew-Burke-Ernzerhof (PBE) [33]. HSE06 [27] calculations including spin-orbit coupling (SOC) were performed for the accurate estimation of band gaps. A plane-wave energy cutoff of 500 eV was used. The Brillouin zone sampling was done by using a Γ -centered k -mesh. For all the compounds, k -meshes of $10 \times 10 \times 10$ (ionic relaxations) and $20 \times 20 \times 20$ (self-consistent-field solutions) were used for PBE calculations. Cell volume, shape, and atomic positions for all the structures were fully relaxed using the conjugate gradient algorithm until the energy (forces) converge(s) to 10^{-6} eV (0.001 eV/ \AA). A tetrahedron method with Blöchl corrections was used for accurate electronic density of states.

Density functional perturbation theory combined with Phonopy [34] was used to obtain relevant phonon properties. The Alloy Theoretic Automated Toolkit [35] was used to generate special quasi random structures (SQS) to simulate the disordered phases of these compounds. The *Ab initio* Scattering and Transport (AMSET) [36] code was used to calculate the electronic transport properties, which uses the variable carrier relaxation time to evaluate the transport distribution function while solving the Boltzmann transport equations. Phono3py [37,38] was used to calculate the lattice thermal conductivity, taking into account the third-order interatomic force constants.

A $2 \times 2 \times 2$ supercell of each structure of the two double half-Heusler alloys are used to simulate the lattice thermal conductivity. The k -meshes used for Brillouin zone integration for the ordered and disordered phases are $12 \times 12 \times 12$ and $6 \times 6 \times 6$, respectively. The mode velocities v_i are calculated by taking the slope of the band corresponding to the vibrational mode at the Γ point. The Debye temperature θ is obtained from the maximum frequency corresponding to the vibrational mode. In addition to v and θ , mode Grüneisen parameters (γ_i) also play a crucial role in dictating the magnitude of lattice thermal transport. The parameter γ is a measure of the degree of anharmonicity of the lattice. The higher the γ value, the more anharmonic the lattice will be; see Refs. [39–42].

A comprehensive list of all these parameters for cubic, tetragonal, and SQS structures for $\text{Zr}_2\text{Ni}_2\text{InSb}$ and $\text{Hf}_2\text{Ni}_2\text{InSb}$ alloys is shown in Table SIII of the Supplemental Material [43].

The electronic thermal conductivity obtained from the solution of the Boltzmann transport equation (using the AMSET code) includes the contribution of the bipolar effect (κ_b). For completeness, we provide separate formulation details here as well. One can evaluate κ_b using the expression [44]

$$\kappa_b = L_b \sigma_i T,$$

where L_b is calculated as

$$L_b = \frac{b}{(1+b)^2}(|S|_e + |S|_h)^2, \quad b = \frac{\sigma_e}{\sigma_h},$$

with subscripts “ e ” and “ h ” standing for electron and hole, respectively. In the first equation σ_i dictates the type of carrier concentrations, $i = e, h$. The bipolar thermal contribution usually becomes important at higher temperatures via the effect of minority charge carriers.

III. RESULTS AND DISCUSSION

A. Crystal structure

Table I shows the optimized lattice constant, the formation energies (ΔE_F), and the relative energies (ΔE) of tetragonal ($I\bar{4}2d$), cubic ($F\bar{4}3m$), and SQS structures ($P1$) of $\text{Hf}_2\text{Ni}_2\text{InSb}$ and $\text{Zr}_2\text{Ni}_2\text{InSb}$. Six different configurations with different site occupations of In and Sb were simulated using the conventional cell of the cubic phase, and the detailed results for the energetically most stable configuration are presented in this paper.

The formation energy is calculated using the expression $\Delta E_F = E_{\text{tot}} - \sum n_i \mu_i$, where E_{tot} is the total energy of the compound per formula unit (f.u.), n_i is the number of atoms of the constituent elements in the compound, and μ_i is the energy per atom of the constituent elements in their respective equilibrium phases. The quite negative values of formation energies (~ 3 eV/f.u.) along with the non-negative acoustic phonon frequencies (shown later in Fig. 4) are already a good criterion for stability. The tetragonal structure of these compounds is theoretically predicted to be stable in the OQMD. The solid-solution phase (represented by SQS structure here) is usually inevitable for this class of compounds at high temperature [26,45]. As such, a comparative study of all these three phases is highly desired to facilitate an in-depth analysis of TE properties in different T ranges.

Interestingly, the energy difference between the two ordered phases is very small (8 meV for Hf-based and 6 meV for Zr-based alloys), whereas the SQS phase is reasonably higher in energy (~ 60 meV) as compared to the ordered phases. Such energy difference is sufficient to

separate the ordered and disordered phases. It also suggests that the solid solution could be a metastable phase and is likely to form at high temperatures where configurational entropy starts to dominate. We further anticipate that long-time annealing at somewhat low temperature (e.g., 800–900 K) could certainly stabilize the ordered phase of these double half-Heuslers [26]. Thus, the study of ordered phases for this class of compounds is equally important as that of the disordered ones. Because there are two distinct ordered phases, the investigation of possible phase transition routes between them is important, since the thermoelectric performance (ZT) can be quite different between these two phases. We have discussed this for one of the double HH alloys, $\text{Zr}_2\text{Ni}_2\text{InSb}$, in Sec. II of the Supplemental Material [43].

Figure 1 shows the theoretically optimized tetragonal, cubic, and SQS structures of $\text{Hf}_2\text{Ni}_2\text{InSb}$ (upper row) and $\text{Zr}_2\text{Ni}_2\text{InSb}$ (lower row). In ordered structures, Hf/Zr and Ni reside on tetrahedral sites whereas In or Sb reside on octahedral sites. The fractional coordinates for the theoretically stable ground-state structures (cubic and tetragonal) are given in Tables SI and SII in the Supplemental Material [43]. A few bond lengths in both the cubic and tetragonal structures are the same, i.e., $d_{\text{Hf-In}} = d_{\text{Hf-Sb}} = 3.05$ Å, $d_{\text{In-Ni}} = 2.68$ Å, $d_{\text{Sb-Ni}} = 2.61$ Å in $\text{Hf}_2\text{Ni}_2\text{InSb}$; and $d_{\text{Zr-In}} = d_{\text{Zr-Sb}} = 3.07$ Å, $d_{\text{In-Ni}} = 2.69$ Å, $d_{\text{Sb-Ni}} = 2.63$ Å in $\text{Zr}_2\text{Ni}_2\text{InSb}$. The $d_{\text{Hf-Ni}}$ bond length in cubic and tetragonal structures for $\text{Hf}_2\text{Ni}_2\text{InSb}$ is 2.61 and 2.64 Å, respectively. Similarly, the $d_{\text{Zr-Ni}}$ bond length in cubic and tetragonal structures for $\text{Zr}_2\text{Ni}_2\text{InSb}$ are 2.63 and 2.66 Å, respectively. In SQS structure, there is large variation in bond length due to randomness, ranging from 2.6 to 6.04 Å.

B. Electronic structure

Figures 2(a) and 2(b) show the band structures of $\text{Hf}_2\text{Ni}_2\text{InSb}$ and $\text{Zr}_2\text{Ni}_2\text{InSb}$, respectively, in their tetragonal phase. Both are direct-band-gap semiconductors with a value of 0.4 and 0.59 eV, respectively. The valence band edges show a dominant contribution from Hf and Ni atoms, whereas the conduction band edges are dominated by Ni atoms for $\text{Hf}_2\text{Ni}_2\text{InSb}$. For $\text{Zr}_2\text{Ni}_2\text{InSb}$, the

TABLE I. Theoretically optimized lattice constants, formation energies (ΔE_F), and relative energy difference (ΔE) of tetragonal, cubic, and SQS structures of $\text{Hf}_2\text{Ni}_2\text{InSb}$ and $\text{Zr}_2\text{Ni}_2\text{InSb}$ alloys.

Compound	Crystal structure	Optimized lattice constants (Å)	ΔE (meV/atom)	ΔE_F (eV/f.u.)
$\text{Hf}_2\text{Ni}_2\text{InSb}$	Tetragonal	$a = b = 6.11, c = 12.24$	0.0	-3.495
	Cubic	$a = b = c = 6.11$	8.0	-3.447
	SQS	$a = 6.09, b = 6.12, c = 5.94$	62.0	-3.120
$\text{Zr}_2\text{Ni}_2\text{InSb}$	Tetragonal	$a = b = 6.14, c = 12.31$	0.0	-3.915
	Cubic	$a = b = c = 6.15$	6.0	-3.875
	SQS	$a = b = 6.18, c = 6.12$	57.1	-3.590

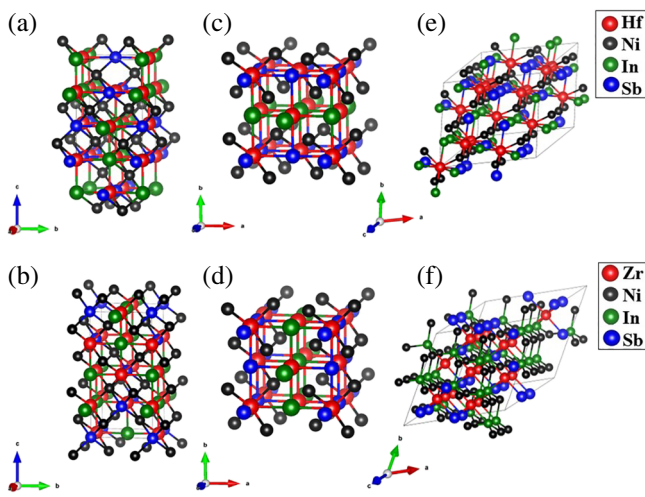


FIG. 1. Theoretically optimized crystal structures of $\text{Hf}_2\text{Ni}_2\text{InSb}$ (upper row) and $\text{Zr}_2\text{Ni}_2\text{InSb}$ (lower row) in the (a),(b) tetragonal, (c),(d) cubic, and (e),(f) SQS phases.

dominant contribution arises from In and Ni atoms near the valence-band edges, whereas the conduction-band edges are mostly composed of Ni. SOC plays a crucial role due to the heavy element Sb, and causes a reduction in the band gap as compared to non-SOC values.

Figures 2(c) and 2(d) show the atom-projected band structure of cubic $\text{Hf}_2\text{Ni}_2\text{InSb}$ and $\text{Zr}_2\text{Ni}_2\text{InSb}$, respectively. For $\text{Hf}_2\text{Ni}_2\text{InSb}$, the conduction bands are mostly

contributed by Hf and Ni atoms, whereas the valence band edges are composed of In and Sb atoms. Multiple valleys are favorable for thermoelectric performance of a compound, as it leads to large band degeneracy. The second conduction band minimum (CBM-2) and third conduction band minimum (CBM-3) lie at an energy difference of 0.03 and 0.05 eV (also contributed by Hf and Ni atoms). For $\text{Zr}_2\text{Ni}_2\text{InSb}$, the conduction bands are mostly contributed by Ni atoms while valence bands by In atoms. The CBM-2 lies at an energy difference of 0.08 eV. This shows large conduction band degeneracy in the cubic phase of these compounds.

The band gap calculated using the (Heyd–Scuseria–Ernzerhof) HSE-SOC functional for Hf- and Zr-based compounds are 0.24 and 0.17 eV, respectively. The former (latter) is an indirect band gap (direct band gap) semiconductor. Figures 2(e) and 2(f) show the band structures of disordered phase for Hf- and Zr-based compounds, respectively. The HSE-SOC band gaps for $\text{Hf}_2\text{Ni}_2\text{InSb}$ and $\text{Zr}_2\text{Ni}_2\text{InSb}$ are 0.06 and 0.05 eV, respectively. Hf atoms have the dominant contribution near valence band edges, while there is a mixed contribution from Hf and Ni atoms near conduction band edges. $\text{Zr}_2\text{Ni}_2\text{InSb}$ has a dominant contribution from the Ni atom, while the valence band edges have mixed contributions from Ni and In atoms.

The ordered structures have larger band gaps as compared to the disordered SQS structures, which can help in suppressing the bipolar effect [46] and hence better electronic transport properties. The ordered tetragonal phase

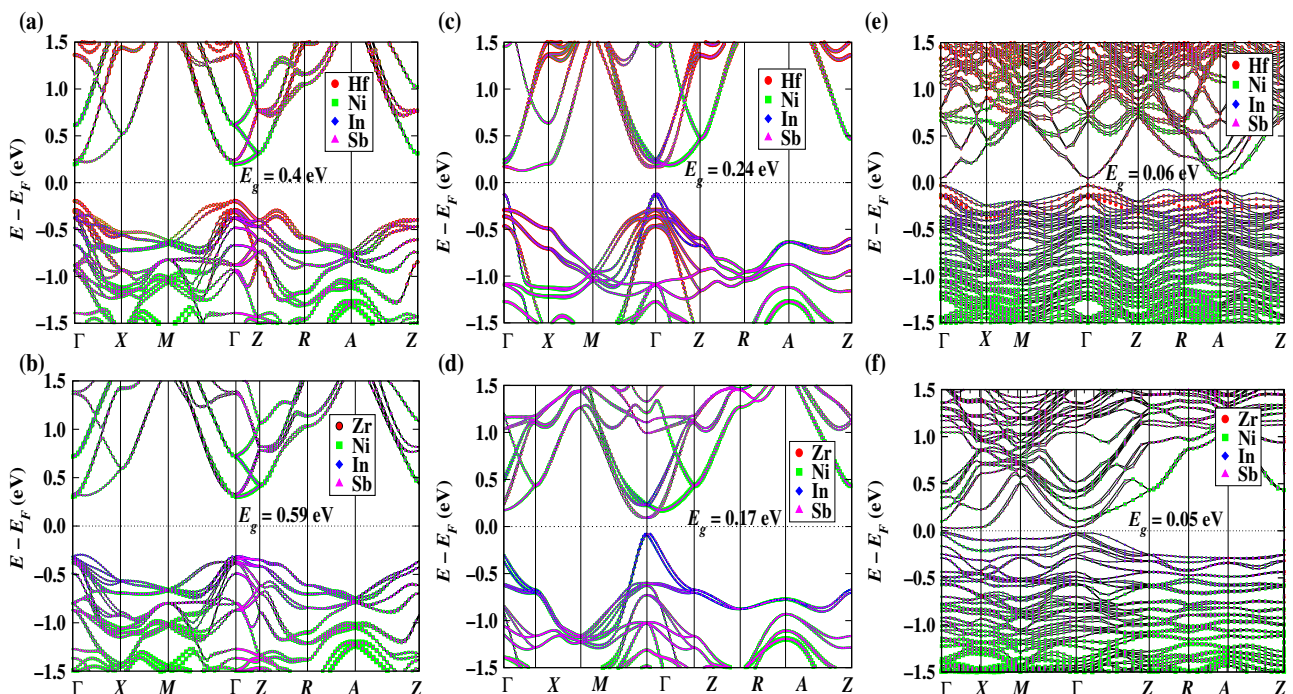


FIG. 2. Atom-projected electronic band structures of (a),(b) tetragonal, (c),(d) cubic, and (e),(f) disordered SQS structures of $\text{Hf}_2\text{Ni}_2\text{InSb}$ (upper row) and $\text{Zr}_2\text{Ni}_2\text{InSb}$ (lower row) alloys.

has the largest band gap, with flat valence bands, which leads to higher density of states effective mass and hence larger *p*-type thermopower, whereas conduction bands for the ordered cubic phase are flat and show multiple valleys at very small energy difference. This indicates better *n*-type thermopower in ordered cubic phase. All the thermoelectric properties are calculated using the PBE band structure with scissor shifted band gap evaluated from the HSE-SOC functional.

C. Electronic transport

The transport parameters of most thermoelectric materials are strongly dependent on carrier relaxation time (τ). Most previous simulations are based on the constant relaxation time approximation [47,48], which is a very crude approximation. The time τ is dictated by different scattering mechanisms such as acoustic scattering, optical scattering, scattering by impurities and defects, and electric polarization in the case of the polar lattice. In the present work, we have estimated the relaxation time for electron and hole transport, using AMSET [36]. AMSET is a numerical code for calculating carrier relaxation time and transport properties within a first-principles framework. We have taken into account all four types of scattering mechanisms in our TE calculations, i.e., acoustic deformation potential, ionized impurity scattering, polar optical phonon scattering, and piezoelectric scattering. We have also captured the effect of charge carrier screening arising out of free carriers at high concentrations. The details of these mechanisms are given in the Supplemental Material [43].

The relaxation time (τ) values of the two compounds in the tetragonal phase are shown in Figs. SII(a,b) and SIII(a,b), respectively, of the Supplemental Material [43]. As can be seen, τ is strongly dependent on both carrier concentration (n) and temperature (T). For $\text{Hf}_2\text{Ni}_2\text{InSb}$, at a high temperature of 900 K, τ varies between 18 and 17 fs for holes and between 40 and 19 fs for electrons. For $\text{Zr}_2\text{Ni}_2\text{InSb}$, τ varies between 18 and 20 fs for holes and between 30 and 20 fs for electrons at 900 K. The τ values for $\text{Hf}_2\text{Ni}_2\text{InSb}$ and $\text{Zr}_2\text{Ni}_2\text{InSb}$ (in the cubic phase) are shown in Figs. SII(c,d) and SIII(c,d) of the Supplemental Material [43], respectively. For $\text{Hf}_2\text{Ni}_2\text{InSb}$, τ varies between 25 and 21 fs for holes and between 35 and 20 fs for electrons with increasing carrier concentration at 900 K. For $\text{Zr}_2\text{Ni}_2\text{InSb}$, τ varies between 24 and 20 fs for holes and between 37 and 22 fs for electrons at 900 K. Thus, the order of magnitude of τ does not vary much, as we go from one phase to the other for ordered phases of a given compound.

The relaxation times (τ) for $\text{Hf}_2\text{Ni}_2\text{InSb}$ and $\text{Zr}_2\text{Ni}_2\text{InSb}$ (in SQS phase) are shown in Figs. SII(e,f) and SIII(e,f) of the Supplemental Material [43], respectively. The τ values range from 60 to 38 fs for holes and from 100 to 34 fs for electrons for $\text{Hf}_2\text{Ni}_2\text{InSb}$ with increasing carrier

concentration at 900 K. For $\text{Zr}_2\text{Ni}_2\text{InSb}$, the τ values range from 75 to 26 fs for electrons and from 46 to 21 fs for holes at 900 K. The individual scattering rates from different scattering mechanisms for all three phases of $\text{Hf}_2\text{Ni}_2\text{InSb}$ and $\text{Zr}_2\text{Ni}_2\text{InSb}$ at 300 K are shown in Figs. SIV and SV of the Supplemental Material [43], respectively. Interestingly, ionized impurity scattering turns out to be the dominant scattering mechanisms in these double half-Heusler alloys. The polar optical phonon scattering is strongly screened by free carriers in the SQS phase. In comparison to the ordered phases, the SQS phase has much lower ionized impurity scattering rates in $\text{Hf}_2\text{Ni}_2\text{InSb}$, which, in turn, yields higher values of relaxation times for the later. In the case of $\text{Zr}_2\text{Ni}_2\text{InSb}$, the scattering rates for the SQS phase are not much smaller than for the ordered phases, which leads to a smaller difference between the relaxation times of SQS and the ordered phases.

Figure 3 shows a comparison of the T -dependent electronic transport properties of Hf- and Zr-based compounds in different phases at a fixed carrier concentration of $1 \times 10^{21} \text{ cm}^{-3}$. The choice of carrier concentration is guided by a previous experimental report on Zr-based double HH alloy [25]. As expected from electronic band structure topology, the *p*-type thermopower of tetragonal structures is larger, whereas for cubic phase, *n*-type thermopower is most promising for both compounds [see Figs. 3(a) and 3(d)]. The SQS phases show lower values of thermopower due to the low band-gap values. The electrical conductivity values for the SQS phase are higher compared to those of the ordered phases due to lower scattering rates in SQS phase. The Hf-based alloy shows quite large values of electrical conductivity due to dispersive conduction bands for the SQS phase. For *p*-type $\text{Hf}_2\text{Ni}_2\text{InSb}$, all the phases show almost similar conductivity values. Similarly, $\text{Zr}_2\text{Ni}_2\text{InSb}$ also shows similar values of conductivity for *n*-type conduction. For *p*-type, the SQS phase shows lowest values of conductivity due to the presence of flat bands.

In the ordered phases, the power factor values for the *p*-type tetragonal phase and *n*-type cubic phase are larger in a large T range [see Figs. 3(c) and 3(g)]. The SQS phase for $\text{Hf}_2\text{Ni}_2\text{InSb}$ shows the largest values of power factor due to significantly dispersive conduction bands and very low value of band gap, whereas the power factor values for $\text{Zr}_2\text{Ni}_2\text{InSb}$ (in SQS phase) are not that high due to the flat nature of the conduction and valence bands. Figures 3(d) and 3(h) show the T dependence of thermal conductivity ($\kappa_e + \kappa_b$) for both compounds, where κ_b is the bipolar thermal conductivity. Minority carriers may be created at high enough temperatures, influencing the conduction mechanism, known as bipolar thermal conduction. The $(\kappa_e + \kappa_b)$ values of SQS structures increase at higher T (around 400–600 K) because of the bipolar component of κ . This is also the reason for the decrease in the Seebeck coefficient at higher T for SQS structures.

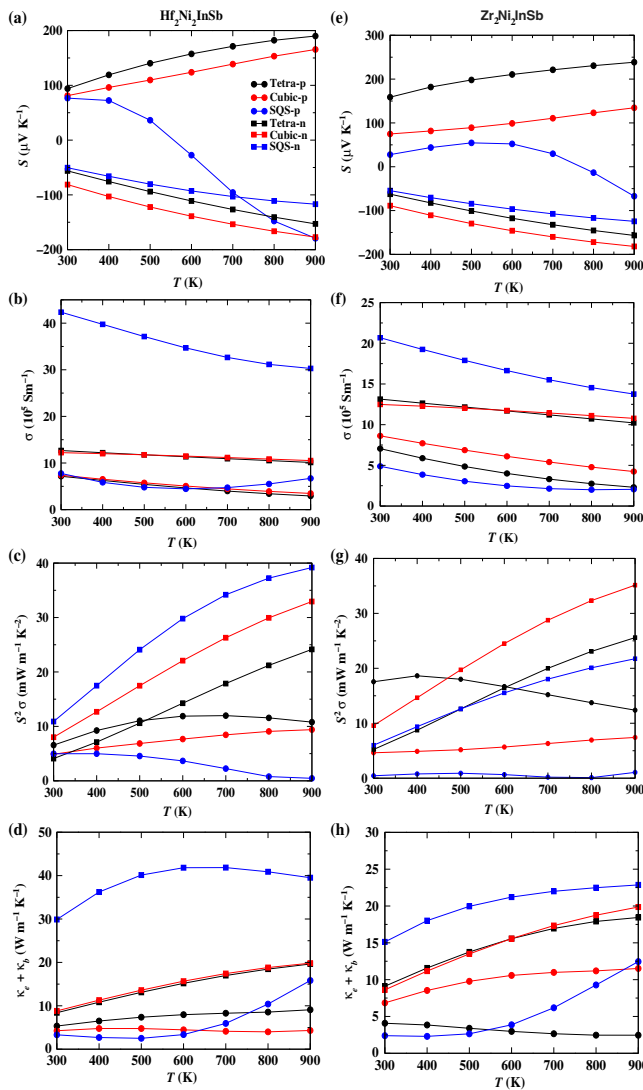


FIG. 3. Temperature dependence of (a),(e) Seebeck coefficient S , (b),(f) electrical conductivity σ , (c),(g) power factor $S^2\sigma$, and (d),(h) electronic thermal conductivity $\kappa_e + \kappa_b$, including both electronic and bipolar contributions. These are shown for p -type (circles) and n -type (squares) conduction in tetragonal (black line), cubic (red line), and SQS (blue line) structures of $\text{Hf}_2\text{Ni}_2\text{InSb}$ (left column) and $\text{Zr}_2\text{Ni}_2\text{InSb}$ (right column) alloys, respectively, at a fixed carrier concentration of $1 \times 10^{21} \text{ cm}^{-3}$.

These double half-Heusler compounds show promising electronic transport properties (large power factor) due to favorable band features. In fact, the present double HH alloys perform better or equivalently to the previously reported Heusler materials. For example, $\text{ZrCoBi}_{0.65}\text{Sb}_{0.15}\text{Sn}_{0.20}$ shows a ZT value of 1.42 at around 970 K [49]. The power factor for this compound is around $3.8 \text{ mW m}^{-1} \text{ K}^{-2}$. Another promising p -type HH compound $\text{FeNb}_{0.8}\text{Ti}_{0.2}\text{Sb}$ shows a ZT value of 1.1 (at around 970 K) [50] with the corresponding power factor of $5.3 \text{ mW m}^{-1} \text{ K}^{-2}$. For n -type HH compounds,

$\text{Ti}_{0.5}\text{Zr}_{0.25}\text{Hf}_{0.25}\text{NiSn}_{0.998}\text{Sb}_{0.002}$ shows a ZT value of 1.5 (at 700 K) [51] and a power factor of $6.2 \text{ mW m}^{-1} \text{ K}^{-2}$.

Further, $\text{Hf}_{0.6}\text{Zr}_{0.4}\text{NiSn}_{0.995}\text{Sb}_{0.005}$ is yet another system with a promising ZT value of 1.2 (at 900 K) [52] and a power factor of $4.7 \text{ mW m}^{-1} \text{ K}^{-2}$. In the double half-Heusler family, $\text{Ti}_4\text{Fe}_2\text{Ni}_2\text{Sb}_4$ (in solid solution) shows a ZT value of 0.5 and 0.4 for p -type and n -type conduction with power factor values of around 1.7 and $1.2 \text{ mW m}^{-1} \text{ K}^{-2}$, respectively, at around 900 K [19]. At the same temperature, the ordered structure for the same compound shows a ZT value of 1.5 for p -type and 0.5 for n -type [26]. The corresponding theoretically calculated power factor values are around 7 and $4 \text{ mW m}^{-1} \text{ K}^{-2}$. $\text{Hf}_2\text{Ni}_2\text{InSb}$ and $\text{Zr}_2\text{Ni}_2\text{InSb}$ (see Fig. 3) show much higher power-factor values in a similar temperature range. $\text{Hf}_2\text{Ni}_2\text{InSb}$ has values of 9.2 (10.7) and 32 (24) $\text{mW m}^{-1} \text{ K}^{-2}$ for p -type and n -type cubic (tetragonal) structure, respectively, while $\text{Zr}_2\text{Ni}_2\text{InSb}$ has values of 7.4 (12) and 35 (25.4) $\text{mW m}^{-1} \text{ K}^{-2}$ for p -type and n -type cubic (tetragonal) structures, respectively. The disordered (SQS) phases also show comparable or better power-factor values (40 $\text{mW m}^{-1} \text{ K}^{-2}$ for Hf-based and 22 $\text{mW m}^{-1} \text{ K}^{-2}$ for Zr-based alloy).

D. Phonons and thermal transport

Figures 4(a) and 4(c), Figs. 4(e) and 4(g), and Figs. 4(i) and 4(k) show the phonon dispersion for tetragonal, cubic, and SQS phases for double HH ($\text{Hf}_2\text{Ni}_2\text{InSb}$, $\text{Zr}_2\text{Ni}_2\text{InSb}$) alloys, respectively. The cubic and tetragonal phases have 6 atoms and 12 atoms in the primitive unit cell, giving rise to 18 and 36 phonon branches, respectively. The SQS phase, on the other hand, has 144 phonon branches. Of them, the lowest three branches correspond to acoustic while the rest correspond to optical branches, respectively. The acoustic branches are further classified into one longitudinal (LA) and two transverse (TA, TA') modes. The velocity of each acoustic mode (v) is calculated from the slope of the band corresponding to the vibrational band at the Γ point. The Debye temperature (θ) can be estimated from the maximum frequency corresponding to the given vibrational mode, within a reasonable approximation.

The Grüneisen parameters for Hf- and Zr-based compounds are shown in Figs. 4(b), 4(f) and 4(j) and in Figs. 4(d), 4(h) and 4(l), respectively. The simulated values of various parameters, namely phonon group velocities (v_i), Debye temperature (θ_i), cell volume (V), atomic mass (M), and Grüneisen parameter (γ_i), for different vibrational modes (LA, TA, TA') for the cubic, tetragonal, and SQS phases of Hf- and Zr-based compounds, are presented in Table SIII of the Supplemental Material [43]. Larger values of γ indicate high degree of anharmonicity. The group velocities of acoustic phonons of double HH alloys are lower compared to their ternary counterparts due to the large mixing of acoustic and optical phonon

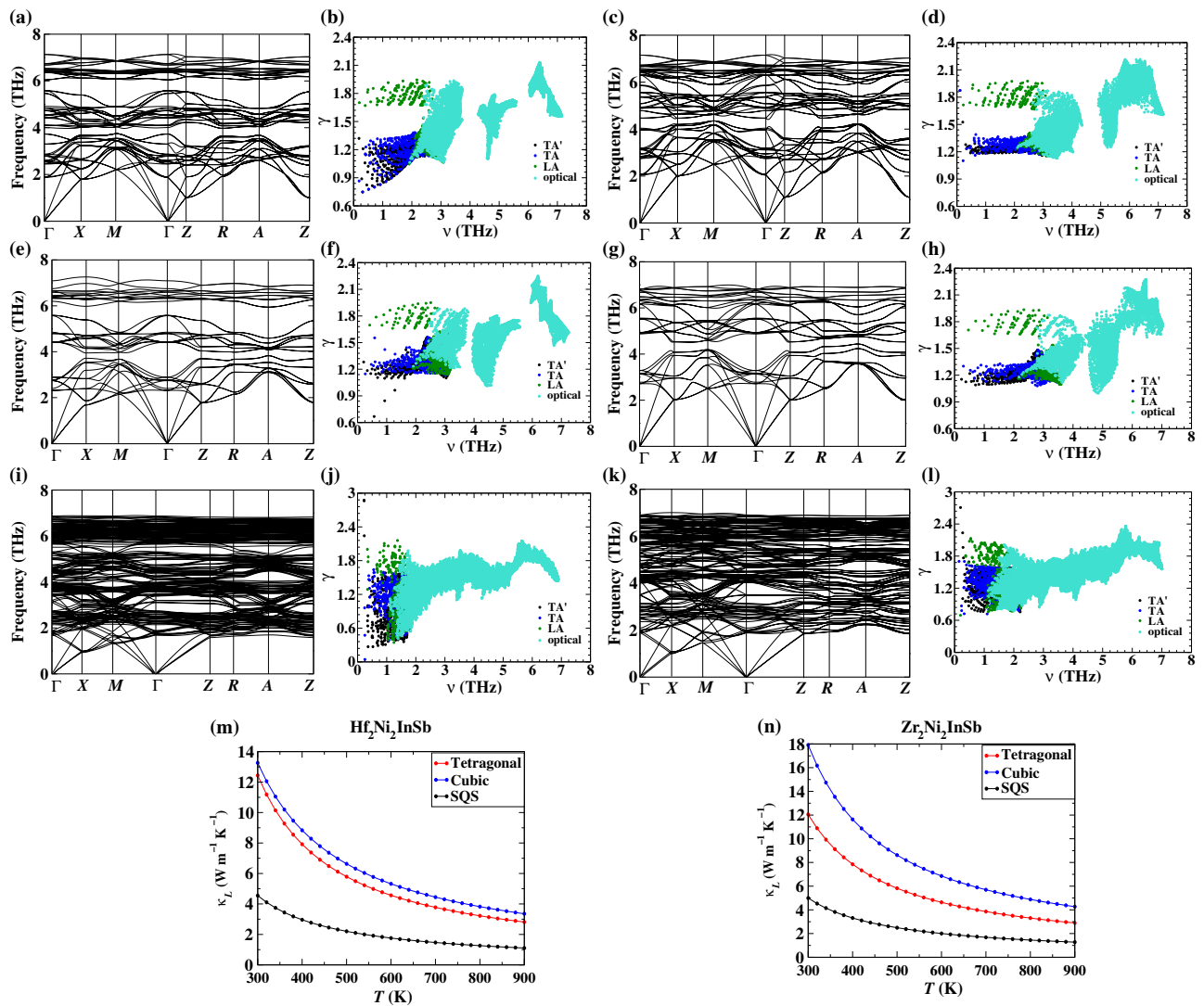


FIG. 4. Phonon dispersion and mode Grüneisen parameter for double HH alloys: (a),(b) tetragonal $\text{Hf}_2\text{Ni}_2\text{InSb}$, (c),(d) tetragonal $\text{Zr}_2\text{Ni}_2\text{InSb}$, (e),(f) cubic $\text{Hf}_2\text{Ni}_2\text{InSb}$, (g),(h) cubic $\text{Zr}_2\text{Ni}_2\text{InSb}$, (i),(j) disordered SQS $\text{Hf}_2\text{Ni}_2\text{InSb}$, and (k),(l) disordered SQS $\text{Zr}_2\text{Ni}_2\text{InSb}$, respectively. (m),(n) Comparison of simulated lattice thermal conductivity κ_L for cubic, tetragonal, and disordered SQS phases of (m) $\text{Hf}_2\text{Ni}_2\text{InSb}$ and (n) $\text{Zr}_2\text{Ni}_2\text{InSb}$ alloys, respectively.

modes in the former. This causes a relative reduction in the lattice thermal conductivity values for double HH alloys.

Figures 4(m) and 4(n) show a comparison of the T dependence of the lattice thermal conductivity (κ_L) for ordered and disordered phases of double HH alloys. The simulated values of κ_L vary from 13.3 to $3.3 \text{ W m}^{-1} \text{ K}^{-1}$ for $\text{Hf}_2\text{Ni}_2\text{InSb}$ (for cubic) and from 12.4 to $2.8 \text{ W m}^{-1} \text{ K}^{-1}$ (for tetragonal) in the temperature range 300–900 K. For $\text{Zr}_2\text{Ni}_2\text{InSb}$, κ_L varies between 17.8 and $4.3 \text{ W m}^{-1} \text{ K}^{-1}$ (for cubic) and between 12.1 and $2.9 \text{ W m}^{-1} \text{ K}^{-1}$ (for tetragonal) in the same T range. The previous theoretically reported room temperature κ_L values for $\text{Zr}_2\text{Ni}_2\text{InSb}$ and $\text{Hf}_2\text{Ni}_2\text{InSb}$ (in tetragonal phase) are 13.58 and $12.5 \text{ W m}^{-1} \text{ K}^{-1}$, respectively, at 300 K [18].

These values agree fairly well with our simulated values. We can see that the lattice thermal conductivity values of double HH alloys in the tetragonal phase are lower than those in the ordered phases, which is useful for enhancing the TE figure of merit (ZT). For the disordered SQS phase, we expect a further reduction of κ_L due to enhanced disorder-induced scattering and our calculations predict the same. The simulated values of κ_L for the SQS phase vary from 4.5 to $1.0 \text{ W m}^{-1} \text{ K}^{-1}$ for $\text{Hf}_2\text{Ni}_2\text{InSb}$ and from 5.0 to $1.1 \text{ W m}^{-1} \text{ K}^{-1}$ for $\text{Zr}_2\text{Ni}_2\text{InSb}$, respectively. Interestingly, despite the high values of κ_L in ordered phases, these alloys show tremendous potential for thermoelectric applications due to their promising electronic transport in ordered phases (see Fig. 3 and further discussion below).

E. Thermoelectric performance

As evident from Fig. 3, the power factor (PF) for these alloys is reasonably high (better than or comparable to the values for some of the best TE materials in the literature [49,52]), indicating their potential for efficient TE performance. In this section, we shall focus on a comparison of the TE figure of merit (ZT) for the n - and p -type conduction of these two alloys. Figure 5 shows the carrier concentration dependence of ZT at different T for p - and n -type conduction of the tetragonal, cubic, and SQS phases of Hf-based (leftmost two columns) and Zr-based (rightmost two columns) alloys. The change in carrier concentration (n) can be thought of as mimicking the effect of doping and/or alloying the host material, keeping the topology of the band structure intact (the so-called rigid-band approximation).

As shown in Figs. 5(a) and 5(b) for the tetragonal phase, the peak values of ZT for $\text{Hf}_2\text{Ni}_2\text{InSb}$ for p -type and n -type conduction occur at carrier concentrations of 6×10^{20} and $2 \times 10^{20} \text{ cm}^{-3}$, respectively. At these values of carrier concentrations, the S_{\max} and PF_{\max} for p -type conduction are $197.3 \mu\text{V K}^{-1}$ and $10.59 \text{ mW m}^{-1} \text{ K}^{-2}$, and for n -type conduction are $270.1 \mu\text{V K}^{-1}$ and $19.48 \text{ mW m}^{-1} \text{ K}^{-2}$,

respectively. This gives a ZT value of ~ 1.36 at 900 K for p -type and ~ 2.02 at 900 K for n -type conduction. For $\text{Zr}_2\text{Ni}_2\text{InSb}$, the peak values of ZT for p -type and n -type conduction are obtained at carrier concentration of 1×10^{21} and $2 \times 10^{20} \text{ cm}^{-3}$, respectively, as shown in Figs. 5(c) and 5(d). The S_{\max} and PF_{\max} for p -type conduction are $238.3 \mu\text{V K}^{-1}$ and $12.35 \text{ mW m}^{-1} \text{ K}^{-2}$ and for n -type conduction are $282.5 \mu\text{V K}^{-1}$ and $20.03 \text{ mW m}^{-1} \text{ K}^{-2}$, respectively. As expected, much higher ZT values of ~ 2.2 and ~ 2.45 at 900 K for p -type and n -type conduction were obtained.

For cubic phase, $\text{Hf}_2\text{Ni}_2\text{InSb}$ shows a peak ZT value of 0.49 for p -type conduction at a carrier concentration of $1 \times 10^{21} \text{ cm}^{-3}$ and 1.51 for n -type conduction at a carrier concentration of $4 \times 10^{20} \text{ cm}^{-3}$ at 900 K, as shown in Figs. 5(e) and 5(f). At these carrier concentrations, the maximum values of simulated Seebeck coefficient (S_{\max}) and power factor (PF_{\max}) are $171.5 \mu\text{V K}^{-1}$ and $9.96 \text{ mW m}^{-1} \text{ K}^{-2}$ for p -type conduction and $248.9 \mu\text{V K}^{-1}$ and $29.6 \text{ mW m}^{-1} \text{ K}^{-2}$ for n -type conduction, respectively. The maximum ZT values for $\text{Zr}_2\text{Ni}_2\text{InSb}$ are 0.44 and 1.82 for p - and n -type conduction at a carrier concentration of 1×10^{21} and $4 \times 10^{20} \text{ cm}^{-3}$, respectively, at 900 K,

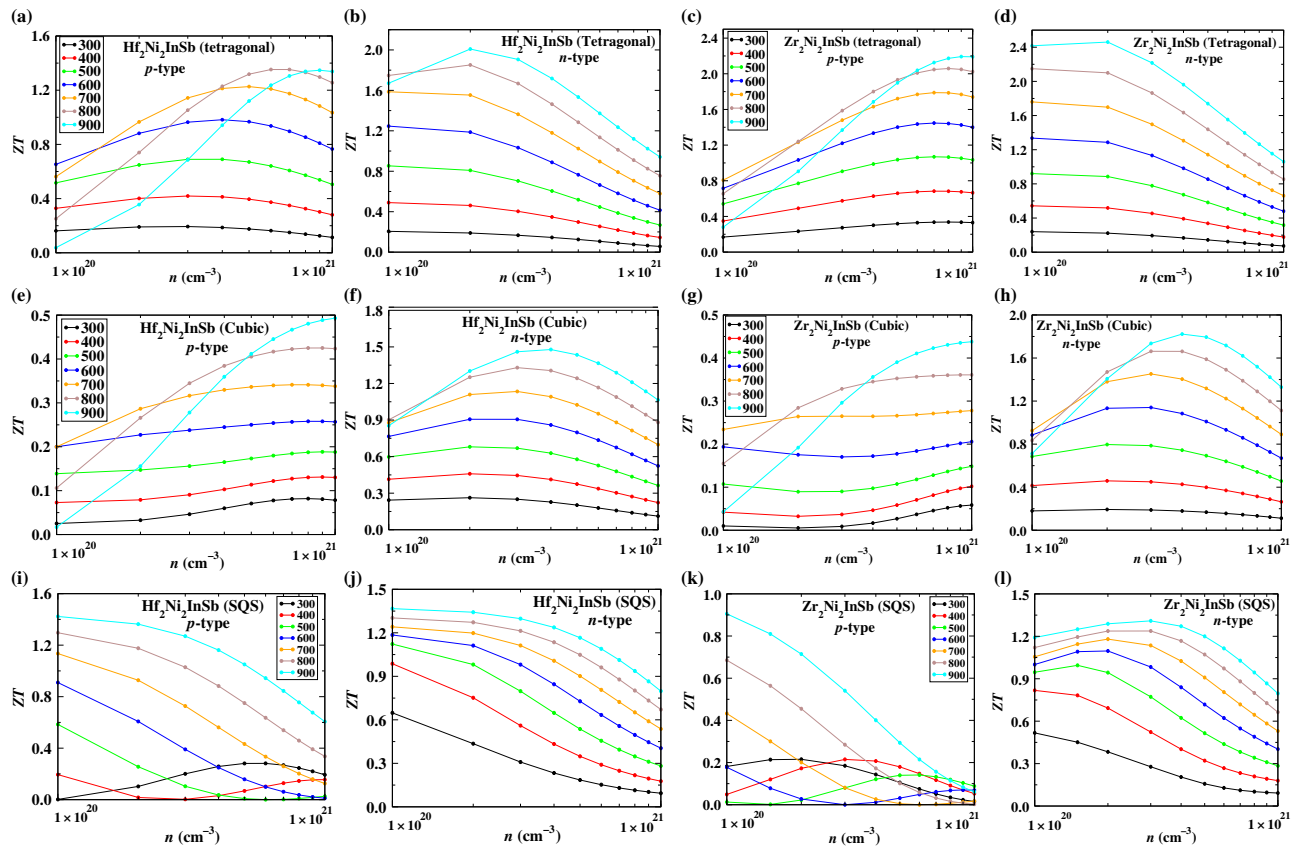


FIG. 5. Thermoelectric figure of merit (ZT) versus carrier concentration (n) at different temperatures (T) for tetragonal (top row), cubic (middle row) and disordered SQS (bottom row) phases of $\text{Hf}_2\text{Ni}_2\text{InSb}$ (leftmost two panels) and $\text{Zr}_2\text{Ni}_2\text{InSb}$ (rightmost two panels) alloys for p -type and n -type conduction, respectively.

as shown in Figs. 5(g) and 5(h). The simulated S_{\max} and PF_{\max} at these carrier concentrations are $134.6 \mu\text{V K}^{-1}$ and $7.41 \text{ mW m}^{-1} \text{ K}^{-2}$ for *p*-type conduction and $250.4 \text{ mW m}^{-1} \text{ K}^{-2}$ and $29.7 \text{ mW m}^{-1} \text{ K}^{-2}$ for *n*-type conduction, respectively.

Although the power factor of these double HH alloys is quite high in the cubic phase for *n*-type conduction, the alloys actually show higher *ZT* value in the tetragonal phase due to the relatively lower values of lattice thermal conductivity. Thus, the reduction of lattice thermal conductivity along with enhanced power factor lead to the improved thermoelectric performance of these double HH compounds as compared to the corresponding 18 VEC ternary HH alloys.

Since the κ_L values of the disordered SQS phases are smaller than those of the ordered phases due to additional disorder-induced scattering, the TE performance of the disordered phase can be high if the electronic transport is favorable. Figures 5(i)–5(l) show the *ZT* values obtained for the SQS phase of the two alloys for *p*-type and *n*-type conduction. As the bipolar contribution is quite evident in *p*-type conduction (see Fig. 3) for the SQS phase, the *ZT* values for *p*-type conduction are reasonably high at high temperatures and low concentrations. For *p*-type conduction, $\text{Hf}_2\text{Ni}_2\text{InSb}$ shows a peak *ZT* value of 1.44 [see Fig. 5(i)] at a carrier concentration of $1 \times 10^{20} \text{ cm}^{-3}$ while $\text{Zr}_2\text{Ni}_2\text{InSb}$ shows a peak *ZT* value of 0.9 at a carrier concentration of $1 \times 10^{20} \text{ cm}^{-3}$ [see Fig. 5(k)]. On the other hand, for *p*-type conduction, $\text{Hf}_2\text{Ni}_2\text{InSb}$ shows a peak *ZT* value of 1.35 [see Fig. 5(j)] at a carrier concentration of $1 \times 10^{20} \text{ cm}^{-3}$ while $\text{Zr}_2\text{Ni}_2\text{InSb}$ shows a peak *ZT* value of 1.30 at a carrier concentration of $3 \times 10^{20} \text{ cm}^{-3}$ [see Fig. 5(l)].

The experimentally reported [25] *ZT* value for *n*-type $\text{Zr}_2\text{Ni}_2\text{InSb}$ is ~ 0.5 via Co and Hf doping at 973 K and $\sim 2 \times 10^{21} \text{ cm}^{-3}$. Interestingly, the experimental report also highlighted a few impurity peaks and/or disorder in their XRD data, and hence their synthesized sample is not purely ordered. One of the main motivations behind our present work is to propose a more careful synthesis of the said compounds to crystallize in the purely ordered phase (cubic or tetragonal), and hence realize better TE performance as demonstrated from our first-principles calculations.

IV. CONCLUSION

Double half-Heusler alloys are formed via the transmutation of two ternary Heusler compounds and hence have higher flexibility for tuning their properties. Here, we report an *ab initio* study of two double half-Heusler alloys, $X_2\text{Ni}_2\text{InSb}$ ($X = \text{Hf}, \text{Zr}$), in their three competing structural phases: tetragonal, cubic, and solid solution. Depending on the structure (ordered or disordered), the simulated band gaps for $\text{Hf}_2\text{Ni}_2\text{InSb}$ lie in the range 0.06–0.4 eV

while those for $\text{Zr}_2\text{Ni}_2\text{InSb}$ are in the range 0.05–0.59 eV. Spin-orbit coupling plays a crucial role in splitting the bands due to the heavy Sb atom. Thermoelectric performance is mostly dominated by the electronic transport in these alloys, with a thermoelectric figure of merit (*ZT*) value as high as 2.02 for *n*-type $\text{Hf}_2\text{Ni}_2\text{InSb}$ and 2.45 for *n*-type $\text{Zr}_2\text{Ni}_2\text{InSb}$ at high temperature. The tetragonal phase shows the most favorable electronic and phonon transport properties, responsible for the highest *ZT*. One of the main motivations of the present work is to propose the synthesis of the purely ordered phase (tetragonal, in particular) of these compounds, which has the potential to facilitate much higher TE performance, unlike disordered or impure samples, as demonstrated in a recent experimental article on $\text{Zr}_2\text{Ni}_2\text{InSb}$ [25]. We expect the present study to receive immediate attention from experimentalists with the possibility to synthesize and cross-validate our findings.

ACKNOWLEDGMENTS

B.S. acknowledges financial support from the Indian Institute of Technology, Bombay, in the form of a teaching assistantship. B.S. acknowledges Vikram for some initial discussions regarding the project. A.A. acknowledges DST-SERB (Grant No. CRG/2019/002050) for funding to support this research.

- [1] T. M. Tritt, Thermoelectrics run hot and cold, *Science* **272**, 1276 (1996).
- [2] F. J. DiSalvo, Thermoelectric cooling and power generation, *Science* **285**, 703 (1999).
- [3] D. Y. Chung, T. H. Hogan, P. Brazis, M. Rocci-Lane, C. Kannewurf, M. Bastae, C. Uher, and M. G. Kanatzidis, CsBi_4Te_6 : A high-performance thermoelectric material for low-temperature applications, *Science* **287**, 1024 (2000).
- [4] R. T. Littleton IV, T. M. Tritt, J. W. Kolis, and D. R. Ketchum, Transition-metal pentatellurides as potential low-temperature thermoelectric refrigeration materials, *Phys. Rev. B* **60**, 13453 (1999).
- [5] G. S. Nolas, M. Kaeser, R. T. Littleton IV, and T. M. Tritt, High figure of merit in partially filled ytterbium skutterudite materials, *Appl. Phys. Lett.* **77**, 1855 (2000).
- [6] B. C. Sales, D. Mandrus, and R. K. Williams, Filled skutterudite antimonides: A new class of thermoelectric materials, *Science* **272**, 1325 (1996).
- [7] J. J. G. Moreno, J. Cao, M. Fronzi, and M. H. N. Assadi, A review of recent progress in thermoelectric materials through computational methods, *Mater. Renew. Sustain. Energy* **9**, 16 (2020).
- [8] L. Huang, Q. Zhang, B. Yuan, X. Lai, X. Yan, and Z. Ren, Recent progress in half-Heusler thermoelectric materials, *Mater. Res. Bull.* **76**, 107 (2016).
- [9] A. L. Pope, T. M. Tritt, M. A. Chernikov, and M. Feuerbacher, Thermal and electrical transport properties of the single-phase quasicrystalline material: $\text{Al}_{70.8}\text{Pd}_{20.9}\text{Mn}_{8.3}$, *Appl. Phys. Lett.* **75**, 1854 (1999).

- [10] Q. Shen, L. Chen, T. Goto, T. Hirai, J. Yang, G. P. Meisner, and C. Uher, Effects of partial substitution of Ni by Pd on the thermoelectric properties of ZrNiSn based half-Heusler compounds, *Appl. Phys. Lett.* **79**, 4165 (2001).
- [11] S. Sakurada and N. Shutoh, Effect of Ti substitution on the thermoelectric properties of (Zr,Hf)NiSn half-Heusler compounds, *Appl. Phys. Lett.* **86**, 082105 (2005).
- [12] C. Yu, T. J. Zhu, R. Z. Shi, Y. Zhang, X. B. Zhao, and J. He, High-performance half-Heusler thermoelectric materials $Hf_{1-x}Zr_xNiSn_{1-y}Sb_y$ prepared by levitation melting and spark plasma sintering, *Acta Mater.* **57**, 2757 (2009).
- [13] Y. Kimura and Y. Tamura, Thermoelectric properties of directionally solidified half-Heusler compound NbCoSn alloys, *Appl. Phys. Lett.* **92**, 012105 (2008).
- [14] Y. Xia, V. Ponnambalam, S. Bhattacharya, A. L. Pope, S. J. Poon, and T. M. Tritt, Electrical transport properties of TiCoSb half-Heusler phases that exhibit high resistivity, *J. Phys.: Condens. Matter* **13**, 77 (2001).
- [15] W. G. Zeier, S. Anand, L. Huang, R. He, H. Zhang, Z. Ren, C. Wolverton, and G. J. Synder, Using the 18-electron rule to understand the nominal 19-electron half-Heusler NbCoSb with Nb vacancies, *Chem. Mater.* **29**, 1210 (2017).
- [16] K. Xia, Y. Liu, S. Anand, G. J. Synder, J. Xin, J. Yu, X. Zhao, and T. Zhu, Enhanced thermoelectric performance in 18-electron $Nb_{0.8}CoSb$ half-Heusler compound with intrinsic Nb vacancies, *Adv. Funct. Mater.* **28**, 1705845 (2018).
- [17] P. Nan, K. Wu, Y. Liu, K. Xia, T. Zhu, F. Lin, J. He, and B. Ge, Direct visualization of spatially correlated displacive short-range ordering in $Nb_{0.8}CoSb$, *Nanoscale* **12**, 21624 (2020).
- [18] S. Anand, M. Wood, Y. Xia, C. Wolverton, and G. J. Synder, Double half-Heuslers, *Joule* **3**, 1226 (2019).
- [19] Z. Liu, S. Guo, Y. Wu, J. Mao, Q. Zhu, H. Zhu, Y. Pei, J. Sui, Y. Zhang, and Z. Ren, Design of high-performance disordered half-Heusler thermoelectric materials using 18-electron rule, *Adv. Funct. Mater.* **29**, 1905044 (2019).
- [20] Q. Wang, X. Li, C. Chen, W. Xue, X. Xie, F. Cao, J. Sui, Y. Wang, X. Liu, and Q. Zhang, Enhanced thermoelectric properties in *p*-type double half-Heusler $Ti_{2-y}Hf_yFeNiSb_{2-x}Sn_x$ compounds, *Phys. Status Solidi A* **217**, 2000096 (2020).
- [21] R. Hasan, T. Park, S.-I. Kim, H.-S. Kim, S. Jo, and K. J. Lee, Enhanced thermoelectric properties of $Ti_{2-y}Hf_yFeNiSb_{2-x}Sn_x$ double half-Heusler compound by Sn doping, *Adv. Energy Sustain. Res.* **3**, 2100206 (2022).
- [22] H. Xie, H. Wang, C. Fu, Y. Liu, G. J. Snyder, X. Zhao, and T. Zhu, The intrinsic disorder related alloy scattering in ZrNiSn half-Heusler thermoelectric materials, *Sci. Rep.* **4**, 6888 (2014).
- [23] X. Ai, B. Lei, M. O. Cichocka, L. Giebel, R. B. Villoro, S. Zhang, C. Scheu, N. Pérez, Q. Zhang, A. Sotnikov *et al.*, Enhancing the thermoelectric properties via modulation of defects in *P*-type MNiSn-based (M = Hf, Zr, Ti) half-Heusler materials, *Adv. Funct. Mater.* **33**, 2305582 (2023).
- [24] R. V. Skolozdra, L. Romaka, L. G. Aksel'rud, G. A. Mel'nik, and Y. T. Tatomin, New phases of MgAgAs, LiGaGe and TiNiSi structural types containing *d*- and *p*-elements, *Inorg. Mater.* **35**, 456 (1999).
- [25] S. He, A. Bahrami, P. Ying, L. Giebel, K. Nielsch, and R. He, Improving the thermoelectric performance of ZrNi(In,Sb)-based double half-Heusler compounds, *J. Mater. Chem. A* **10**, 13476 (2022).
- [26] S. Guo, Z. Liu, Z. Feng, T. Jia, S. Anand, G. J. Snyder, and Y. Zhang, Prediction of improved thermoelectric performance by ordering in double half-Heusler materials, *J. Mater. Chem. A* **8**, 23590 (2020).
- [27] A. V. Kruckau, O. A. Vydriv, A. F. Izmaylov, and G. E. Scuseria, Influence of the exchange screening parameter on the performance of screened hybrid functionals, *J. Chem. Phys.* **125**, 224106 (2006).
- [28] G. Kresse and J. Furthmüller, Efficiency of ab-initio total energy calculations for metals and semiconductors using a plane-wave basis set, *Comput. Mater. Sci.* **6**, 15 (1996).
- [29] G. Kresse and J. Furthmüller, Efficient iterative schemes for *ab initio* total-energy calculations using a plane-wave basis set, *Phys. Rev. B* **54**, 011169 (1996).
- [30] G. Kresse and J. Hafner, *Ab initio* molecular dynamics for liquid metals, *Phys. Rev. B* **47**, 558 (1993).
- [31] P. Hohenberg and W. Kohn, Inhomogeneous electron gas, *Phys. Rev.* **136**, B865 (1964).
- [32] P. E. Blöchl, Projector augmented-wave method, *Phys. Rev. B* **50**, 17953 (1994).
- [33] J. P. Perdew, K. Burke, and M. Ernzerhof, Generalized gradient approximation made simple, *Phys. Rev. Lett.* **77**, 3865 (1996).
- [34] A. Togo and I. Tanaka, First principles phonon calculations in materials science, *Scr. Mater.* **108**, 1 (2015).
- [35] A. Van de Walle, P. Tiwary, M. D. Jong, D. Olmsted, M. Asta, A. Dick, D. Shin, Y. Wang, L.-Q. Chen, and Z.-K. Liu, Efficient stochastic generation of special quasirandom structures, *Calphad* **42**, 13 (2013).
- [36] A. M. Ganose, J. Park, A. Faghaninia, R. Woods-Robinson, K. A Persson, and A. Jain, Efficient calculation of carrier scattering rates from first principles, *Nat. Commun.* **12**, 2222 (2021).
- [37] Atsushi Togo, Laurent Chaput, and Isao Tanaka, Distributions of phonon lifetimes in Brillouin zones, *Phys. Rev. B* **91**, 094306 (2015).
- [38] Atsushi Togo, First-principles phonon calculations with Phonopy and Phono3py, *J. Phys. Soc. Jpn.* **92**, 012001 (2023).
- [39] Y. Zhang, First-principles Debye–Callaway approach to lattice thermal conductivity, *J. Materiomics* **2**, 237 (2016).
- [40] Vikram, J. Kangsabanik, Enamullah, and Aftab Alam, Bismuth based half-Heusler alloys with giant thermoelectric figures of merit, *J. Mater. Chem. A* **5**, 6131 (2017).
- [41] Vikram, B. Sahni, C. K. Barman, and Aftab Alam, Accelerated discovery of new 8-electron half-Heusler compounds as promising energy and topological quantum materials, *J. Phys. Chem. C* **123**, 7074 (2019).
- [42] Bhawna Sahni, Vikram, J. Kangsabanik, and Aftab Alam, Reliable prediction of new quantum materials for topological and renewable-energy applications: A high-throughput screening, *J. Phys. Chem. Lett.* **15**, 6364 (2020).
- [43] See Supplemental Material at <http://link.aps.org/supplemental/10.1103/PhysRevApplied.22.034034> for auxiliary information on the ground-state structures for the ordered double half-Heusler alloys Hf_2Ni_2InSb and Zr_2Ni_2InSb , and corresponding phase transition route between the two phases in the latter compound. Also, we report several

- properties calculated from phonon calculations, the formalism for carrier relaxation time, and the corresponding scattering rates and relaxation time data for both ordered and disordered phases of the two alloys.
- [44] H. Muta, T. Kanemitsu, K. Kurosaki, and S. Yamanaka, Substitution effect on thermoelectric properties of ZrNiSn based half-Heusler compounds, *Mater. Trans.* **47**, 1453 (2016).
 - [45] X. Xu, Y. Liu, W. Fang, S. Teng, J. Wang, F. He, Y. Wang, F. Yin, J. Li, and J. Li, Improved thermoelectric properties of doped $\text{A}_{0.5}\text{B}_{0.5}\text{NiSn}$ ($\text{A}, \text{B} = \text{Ti}, \text{Zr}, \text{Hf}$) with a special quasirandom structure, *J. Mater. Sci.* **56**, 4280 (2021).
 - [46] J. J. Gong, A. J. Hong, J. Shuai, L. Li, Z. B. Yan, Z. F. Ren, and J.-M. Liu, Investigation of the bipolar effect in the thermoelectric material CaMg_2Bi_2 using a first principles study, *Phys. Chem. Chem. Phys.* **18**, 16566 (2016).
 - [47] J. Yang, H. Li, T. Wu, W. Zhang, L. Chen, and J. Yang, Evaluation of half-Heusler compounds as thermoelectric materials based on the calculated electrical transport properties, *Adv. Funct. Mater.* **18**, 2880 (2008).
 - [48] W. Chen, J.-H. Pohls, G. Hautier, D. Broberg, S. Bajaj, U. Aydemir, Z. M. Gibbs, H. Zhu, M. Asta, G. J. Synder *et al.*, Understanding thermoelectric properties from high-throughput calculations: Trends, insights, and comparisons with experiment, *J. Mater. Chem. C* **4**, 4414 (2016).
 - [49] H. Zhu, R. He, J. Mao, Q. Zhu, C. Li, J. Sun, W. Ren, Y. Wang, Z. Liu, Z. Tang, A. Sotnikov, Z. Wang, D. Broido, D. J. Singh, G. Chen, K. Nielsch, and Z. Ren, Discovery of ZrCoBi based half Heuslers with high thermoelectric conversion efficiency, *Nat. Commun.* **9**, 2497 (2018).
 - [50] R. He, D. Kraemer, J. Mao, L. Zeng, Q. Jie, Y. Lan, C. Li, J. Shuai, H. S. Kim, Y. Liu, D. Broido, C.-W. Chua, G. Chen, and Z. Ren, Achieving high power factor and output power density in *p*-type half-Heuslers $\text{Nb}_{1-x}\text{Ti}_x\text{FeSb}$, *PNAS* **113**, 13576 (2016).
 - [51] N. Shutoh and S. Sakurada, Thermoelectric properties of the $\text{Ti}_X(\text{Zr}_{0.5}\text{Hf}_{0.5})_{1-X}\text{NiSn}$ half-Heusler compounds, *J. Alloys Compd.* **389**, 204 (2005).
 - [52] L. Chen, S. Gao, X. Zeng, A. M. Dehkordi, T. M. Tritt, and S. J. Poon, Uncovering high thermoelectric figure of merit in $(\text{Hf}, \text{Zr})\text{NiSn}$ half-Heusler alloys, *Appl. Phys. Lett.* **107**, 041902 (2015).